A Synchronous Reference Frame Robust Predictive Current Control for Three-Phase Grid-Connected Inverters

José M. Espí Huerta, *Member, IEEE*, Jaime Castelló-Moreno, *Student Member, IEEE*, Jonatan Roberto Fischer, and Rafael García-Gil

***Abstract*—This paper presents a new predictive current control for three-phase grid-connected inverters in the synchronous reference frame. The control combines a deadbeat control law with a diagonal Luenberger observer to estimate the future value of the grid currents. It provides a decoupled control of the active and reactive power and offers robustness against the computational delay inherent in the digital implementation and against filter and grid-impedance uncertainties. This control exhibits a very fast current response while widely improving the gain and phase margins of the traditional predictive controllers.**

***Index Terms*—Current-controlled voltage-source inverter (CC-VSI), robust predictive current control (RPCC).**

I. Introduction

MOST distributed-energy systems [1]–[3] are interfaced to the utility grid through a current-controlled voltage-source inverter (CC-VSI) (Fig. 1) [4]–[8].

The CC-VSI control circuit has two missions [9], [10]: regulate the dc-bus voltage and transfer the generated power to the grid as an ac current with low harmonic distortion and controlled displacement factor [9]. The CC-VSI control is usually a double-loop structure: an outer voltage loop to regulate the dc-bus voltage and an inner current loop which performs the current tracking according to the reference signals (Fig. 1).

With regard to the current loop, fast current controls have the benefits of a reduced dc-bus capacitance and the chance of a higher voltage-loop bandwidth. Among all fast current controllers, it is known that deadbeat or predictive controllers [10]–[17] offer the fastest response. Moreover, they include a feedforward compensation for the grid voltage, which immediately compensates for grid-voltage harmonics or fast variations, such as dip voltages.

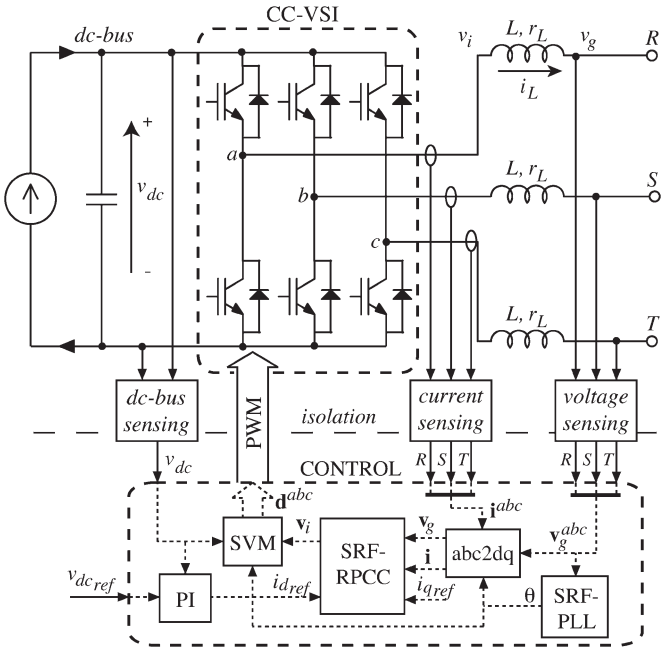

Fig. 1. CC-VSI with isolated neutral point and the proposed SRF-RPCC control.

However, due to their high bandwidth, the stability of deadbeat controllers is often compromised by the calculation delay inherent in the digital implementation or variations on the filtering inductance [18].

Recently, published predictive controllers [10]–[12] have tolerated a maximum inductance reduction of 50% of their nominal value and a maximum control delay of less than two sampling periods. These limits were overcome in [19] in the stationary or abc reference frame.

This paper presents a new robust predictive current controller (RPCC) in the rotating or synchronous reference frame (SRF) (SRF-RPCC) that offers robustness against these two factors, enhancing the stability margins of the traditional predictive controllers while maintaining the fast response typical of a deadbeat controller. The presented stability analysis and the experimental results show that the RPCC tolerates delays beyond two sampling periods and considerably improves the previous tolerance against inductance variations.

Manuscript received January 29, 2009; revised April 6, 2009 and May 13, 2009. First published August 7, 2009; current version published February 10, 2010.

J. M. Espí Huerta, J. Castelló-Moreno, and R. García-Gil are with the Department of Electrical Engineering, University of Valencia, 46100 Burjassot-Valencia, Spain (e-mail: Jose.M.Espi@uv.es; Jaime.Castello@uv.es; Rafael.Garcia-Gil@uv.es).

J. R. Fischer is with the Laboratorio de Instrumentación y Control (LIC), Universidad Nacional de Mar de Plata and CONICET, 7600 Mar del Plata, Argentina (e-mail: jfischer@fi.mdp.edu.ar).

Digital Object Identifier 10.1109/TIE.2009.2028815

II. Modeling of the Power Stage

A. Basic Model

In the stationary reference frame or abc-frame, the dynamics of the three filtered currents i_a, i_b, i_c are given by

$$\frac{d}{dt}\mathbf{i}^{abc} = \frac{-r_L}{L}\cdot\mathbf{i}^{abc} + \frac{1}{L}\cdot\mathbf{v}^{abc} \tag{1}$$

where $\mathbf{i}^{abc} = [i_a, i_b, i_c]^T$, r_L is the equivalent series resistance of the filtering inductors, and $\mathbf{v}^{abc} = [v_a, v_b, v_c]^T$ is the vector of averaged voltages applied to the inductors, i.e.,

$$\mathbf{v}^{abc} = \mathbf{v}_i^{abc} - \mathbf{v}_g^{abc} \tag{2}$$

$\mathbf{v}_i^{abc}$ being the vector of averaged inverter voltages and $\mathbf{v}_g^{abc}$ the vector of grid voltages.

In the rotating SRF, the current and voltage vectors are transformed as $\mathbf{i} \equiv [i_d, i_q]^T = \mathbf{T}_{abc2dq}\cdot\mathbf{i}^{abc}$ and $\mathbf{v} \equiv [v_d, v_q]^T = \mathbf{T}_{abc2dq}\cdot\mathbf{v}^{abc}$, where $\mathbf{T}_{abc2dq}$ is the Park's transform matrix, and, thus, (1) becomes

$$\frac{d}{dt}\mathbf{i} = \mathbf{A}\cdot\mathbf{i} + \mathbf{B}\cdot\mathbf{v} \tag{3}$$

where $\mathbf{v} = \mathbf{v}_i - \mathbf{v}_g$, $\mathbf{v}_i = [v_{i_d}, v_{i_q}]^T$, $\mathbf{v}_g = [v_{g_d}, v_{g_q}]^T$

$$\mathbf{A} = \begin{pmatrix} \frac{-r_L}{L} & \omega_l \\ -\omega_l & \frac{-r_L}{L} \end{pmatrix} \qquad \mathbf{B} = \frac{1}{L}\cdot\mathbf{I}$$

ω_l is the line frequency, and $\mathbf{I}$ is the 2×2 identity matrix.

It is assumed that (3) is invariant, and, therefore, the transition matrix is

$$\Phi(t) \equiv e^{\mathbf{A}t} = e^{\frac{-r_L}{L}t}\cdot\begin{pmatrix} \cos\omega_l t & \sin\omega_l t \\ -\sin\omega_l t & \cos\omega_l t \end{pmatrix}. \tag{4}$$

The plant (3) is seen by the control as discretized with sampling period T, with a discrete state equation

$$\mathbf{i}(k+1) = \mathbf{A}_d\cdot\mathbf{i}(k) + \mathbf{B}_d\cdot\mathbf{v}(k) \tag{5}$$

where

$$\mathbf{A}_d = \Phi(T) \qquad \mathbf{B}_d = \mathbf{A}^{-1}(\mathbf{A}_d - \mathbf{I})\mathbf{B}. \tag{6}$$

B. Modeling With Control Delay

An ideal controller would sample, calculate, and transfer its output, all at the same instant kT. Of course, in practice, this is not possible because control calculations consume a certain time. Let us suppose the acquisitions are finished a time t_d before the pulsewidth modulation (PWM) update instant kT, as shown in Fig. 2. Sampling can be performed either before the calculation interval [12], [15], [20] (point A in Fig. 2, where $t_d > T$), or during the calculation interval [11] (point B in Fig. 2, where $t_d < T$). The last case is the most similar to the ideal control, but it leaves a small spare time for calculations. Both cases are regarded by defining a time delay $t_d = T_d + m\cdot T$, with $T_d < T$ and $m = \{0, 1\}$. Obviously, each analog acquisition channel would be affected by a slightly different time t_d.

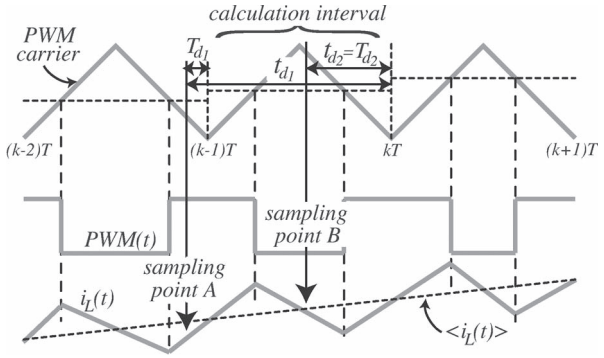

Fig. 2. Sampling options: (point A) before the calculation interval or (point B) during the calculation interval.

Sampling a signal a time t_d before the instant kT is equivalent to sampling at instant kT when the signal is delayed a time t_d. Therefore, the control performs equivalently as acquiring, at instants kT, the delayed currents $\mathbf{i}'(t) \equiv \mathbf{i}(t-t_d)$ and grid voltages $\mathbf{v}_g'(t) \equiv \mathbf{v}_g(t-t_d)$.

Introducing a time delay t_d in the general solution of the continuous state equation (3) results in

$$\mathbf{i}'(t) = \mathbf{i}(t-t_d) = e^{\mathbf{A}(t-t_d-t_0)}\cdot\mathbf{i}(t_0) + \int_{t_0}^{t-t_d} e^{\mathbf{A}(t-t_d-\tau)}\mathbf{B}\mathbf{v}(\tau)d\tau \tag{7}$$

and letting $t_0 = kT - t_d$ and $t = (k+1)T$, it follows that

$$\mathbf{i}'(k+1) = \mathbf{A}_d\cdot\mathbf{i}'(k) + \int_{kT-t_d}^{(k+1)T-t_d} e^{\mathbf{A}((k+1)T-t_d-\tau)} \times \mathbf{B}\left(\mathbf{v}_i(\tau) - \mathbf{v}_g(\tau)\right)d\tau. \tag{8}$$

In the SRF, $\mathbf{v}_g$ is slowly time varying, being almost constant during a sampling period. Hence,

$$\int_{kT-t_d}^{(k+1)T-t_d} e^{\mathbf{A}((k+1)T-t_d-\tau)}\mathbf{B}\mathbf{v}_g(\tau)d\tau \approx \mathbf{B}_d\cdot\mathbf{v}_g'(k). \tag{9}$$

As $\mathbf{v}_i$ is constant between two sampling instants, it follows that

$$\int_{kT-t_d}^{(k+1)T-t_d} e^{\mathbf{A}((k+1)T-t_d-\tau)}\mathbf{B}\mathbf{v}_i(\tau)d\tau = \mathbf{B}_{d_1}\cdot\mathbf{v}_i(k-1-m) + \mathbf{B}_{d_0}\cdot\mathbf{v}_i(k-m) \tag{10}$$

where

$$\begin{aligned}\mathbf{B}_{d_0} &= \mathbf{A}^{-1}\cdot(\Phi(T-T_d) - \mathbf{I})\cdot\mathbf{B} \\ \mathbf{B}_{d_1} &= \mathbf{A}^{-1}\cdot(\mathbf{A}_d - \Phi(T-T_d))\cdot\mathbf{B} = \mathbf{B}_d - \mathbf{B}_{d_0}.\end{aligned} \tag{11}$$

Substituting (9) and (10) into (8), the discrete model of the power stage results, instead of (5)

$$\mathbf{i}'(k+1) = \mathbf{A}_d\cdot\mathbf{i}'(k) - \mathbf{B}_d\cdot\mathbf{v}_g'(k) + \mathbf{B}_{d_1}\cdot\mathbf{v}_i(k-1-m) + \mathbf{B}_{d_0}\cdot\mathbf{v}_i(k-m). \tag{12}$$

III. SRF-RPCC

The sampling instant of a digital control is traditionally set before the calculation interval (point A in Fig. 2) in order to arrange the whole next sampling period to solve the control calculations. In particular, the analog to digital conversions are frequently processed in parallel with the calculations of the previous interval, setting the instant for the three current acquisitions just before the ending of the previous interval at $(k-1)T$. In this way, there is $m=1$, $T_d \ll T$. This has the additional advantage that, if using a centered PWM modulation, the current sensed is approximately the averaged current (see Fig. 2) without the need of using filters.

Taking $m=1$, $T_d \approx 0$ in (12), we obtain

$$\mathbf{i}'(k+1) = \mathbf{A}_d \cdot \mathbf{i}'(k) + \mathbf{B}_d \cdot \left[\mathbf{v}_i(k-1) - \mathbf{v}'_g(k)\right]. \quad (13)$$

Applying an advance of a sampling period to the previous equation and letting $\mathbf{i}'(k+2) = \mathbf{i}_{ref}(k)$, we get the two-sample deadbeat control law

$$\mathbf{v}_i(k) = \mathbf{B}_m^{-1} \cdot [\mathbf{i}_{\rm ref}(k) - \mathbf{A}_m \cdot \mathbf{i}'(k+1)] + \mathbf{v}'_g(k+1) \quad (14)$$

also known as "predictive" because it needs a prediction for the future values $\mathbf{i}'(k+1)$ and $\mathbf{v}'_g(k+1)$. In the previous equation, $\mathbf{B}_m \equiv \mathbf{B}_d(L_m)$, $\mathbf{A}_m \equiv \mathbf{A}_d(L_m)$ are the programmed control matrices, L_m being the measured value of the filtering inductance. Notice that while L_m is constant, the actual inductance L can vary with time, for instance when operating close to saturation [18].

The proposed SRF-RPCC utilizes a Luenberger observer to predict $\mathbf{i}'(k+1)$, with

$$\widehat{\mathbf{i}}'(k+1) = (\mathbf{A}_m - \mathbf{L}_d) \cdot \widehat{\mathbf{i}}'(k) + \mathbf{L}_d \cdot \mathbf{i}'(k) + \mathbf{B}_m \cdot \left[\mathbf{v}_i(k-1) - \mathbf{v}'_g(k)\right] \quad (15)$$

where $\widehat{\mathbf{i}}'(k)$ is the estimation of $\mathbf{i}'(k)$ and $\mathbf{L}_d$ is the observer matrix gain. Notice that the conventional predictive control is a particular case for $\mathbf{L}_d \to \mathbf{A}_m$. Of course, $\mathbf{L}_d$ must be designed so that all eigenvalues of $\mathbf{A}_m - \mathbf{L}_d$ lie inside the unit circle.

To predict $\mathbf{v}'_g(k+1)$, it is assumed that three consecutive acquisitions of $\mathbf{v}'_g(k)$ are equally spaced, which gives

$$\mathbf{v}'_g(k+1) \approx 2 \cdot \mathbf{v}'_g(k) - \mathbf{v}'_g(k-1). \quad (16)$$

IV. Dynamic Analysis of the SRF-RPCC

A. Deadbeat Performance

The block diagram of the SRF-RPCC and its simplification are shown in Fig. 3. The control can be reduced to a unity-feedback structure with the controller

$$G_c(z) = \mathbf{B}_m^{-1} \cdot \mathbf{A}_m \cdot (z\mathbf{I} + \mathbf{L}_d)^{-1} \cdot \mathbf{L}_d z \quad (17)$$

and the prefilter

$$G_p(z) = \mathbf{L}_d^{-1} \cdot \left[\mathbf{I} - (\mathbf{A}_m - \mathbf{L}_d) z^{-1}\right] \cdot \mathbf{A}_m^{-1}. \quad (18)$$

Notice that (16) is a feedforward input to the control. The inverter's modulation $\mathbf{v}_i(k)$ contains a "copy" of the grid voltage, to be cancelled at both ends of the filtering inductors. This makes the inverter currents unaffected by grid-voltage variations or distortions.

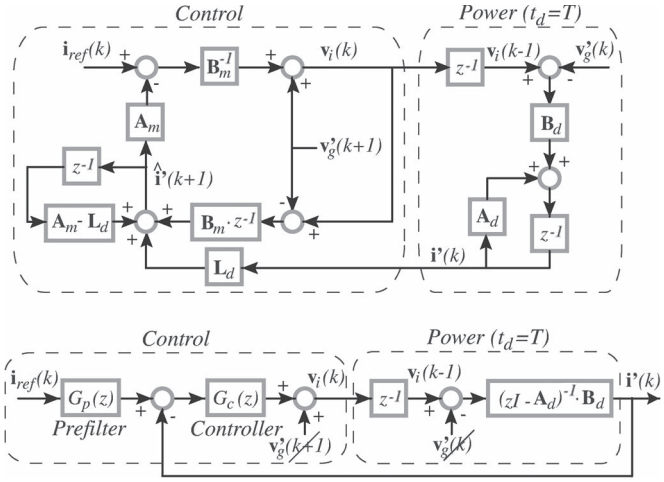

Fig. 3. Block diagram of the proposed SRF-RPCC and its simplification, when the control delay is $t_d \approx T$.

From Fig. 3, the transfer matrix of the loop for $t_d \approx T$ is

$$H(z) = (z\mathbf{I} - \mathbf{A}_d)^{-1}\mathbf{B}_d\mathbf{B}_m^{-1}\mathbf{A}_m(z\mathbf{I} + \mathbf{L}_d)^{-1}\mathbf{L}_d. \quad (19)$$

When the actual inductance L is similar to the programmed inductance L_m, it follows that $\mathbf{A}_d \approx \mathbf{A}_m$, $\mathbf{B}_d \approx \mathbf{B}_m$, and, therefore, the closed-loop transfer matrix is

$$\begin{aligned} F(z) &= H(\mathbf{I}+H)^{-1}G_p = \left[G_p^{-1}(\mathbf{I}+H^{-1})\right]^{-1} \\ &= \left(G_p^{-1}z^2G_p\right)^{-1} = z^{-2}\cdot\mathbf{I} \end{aligned} \quad (20)$$

indicating that the control is a two-sample deadbeat (stabilizes in only two sampling periods) for any observer gain $\mathbf{L}_d$ such that G_p^{-1} (or the observer) is stable. Obviously, the deadbeat performance degrades when $L_m \neq L$ or $t_d \neq T$.

B. Equivalent SISO Control

In most cases, the sampling period is small enough to satisfy

$$\cos\omega_l T \approx 1 \quad \sin\omega_l T \approx \omega_l T \quad e^{\frac{-r_L}{L}T} \approx 1 - \frac{r_L}{L}T \quad (21)$$

and then the transition matrix for $t \leq T$ can be expressed as

$$\Phi(t) \approx \begin{pmatrix} 1-\frac{r_L}{L}t & \omega_l t \\ -\omega_l t & 1-\frac{r_L}{L}t \end{pmatrix}. \quad (22)$$

Therefore,

$$\mathbf{A}_d \approx \begin{pmatrix} 1-\frac{r_L}{L}T & \omega_l T \\ -\omega_l T & 1-\frac{r_L}{L}T \end{pmatrix} \quad (23)$$

$$\mathbf{B}_d \approx \mathbf{B}\cdot T = \frac{T}{L}\cdot\mathbf{I} \qquad \mathbf{B}_m \approx \frac{T}{L_m}\cdot\mathbf{I} \quad (24)$$

and (11) reduces to

$$\begin{aligned} \mathbf{B}_{d_1} &\approx \mathbf{B}\cdot T_d = \frac{T_d}{L}\cdot\mathbf{I} \\ \mathbf{B}_{d_0} &\approx \mathbf{B}\cdot(T-T_d) = \frac{T-T_d}{L}\cdot\mathbf{I}. \end{aligned} \quad (25)$$

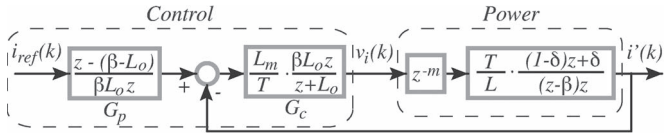

Fig. 4. Equivalent SISO control to simplify the dynamic analysis.

Moreover, when sampling frequencies are above 3 kHz, the small cross-coupling terms in $\mathbf{A}_d$ can be neglected ($\omega_l T < 0.1$ for a 50-Hz grid), i.e.,

$$\mathbf{A}_d \approx \mathbf{A}_m \approx \beta \cdot \mathbf{I} \tag{26}$$

where $\beta = e^{(-r_L/L)T}$, and the discrete model of the power stage (12) approximates the decoupled system

$$\mathbf{i}'(k+1) \approx \beta \cdot \mathbf{i}'(k) + \frac{T}{L}\big[\delta \mathbf{v}_i(k-1-m) + (1-\delta)\mathbf{v}_i(k-m) - \mathbf{v}'_g(k)\big] \tag{27}$$

where $\delta = T_d/T < 1$. The transfer matrix from $\mathbf{v}_i$ to $\mathbf{i}'$ is

$$H_i(z) \approx \frac{T/L}{z-\beta} \cdot \left[\frac{(1-\delta)\cdot z + \delta}{z^{m+1}}\right] \cdot \mathbf{I} \tag{28}$$

presenting a zero at $z = -\delta/(1-\delta)$. The zero lies outside the unit circle if $\delta > 0.5$, that is, if $T_d > T/2$.

If a scalar matrix $\mathbf{L}_d$ is chosen, i.e.,

$$\mathbf{L}_d = L_o \cdot \mathbf{I} \tag{29}$$

where L_o is a scalar value between 0 and $\beta \approx 1$ and (24) and (26) are taken into account, the control in Fig. 3 becomes decoupled into two identical single-input–single-output (SISO) controls, one for the d-coordinate and the other for the q-coordinate. Fig. 4 shows the resulting equivalent SISO control for each coordinate. Notice that the ratio L_m/L acts as a gain in the loop and that $G_p(z)$ is a derivative prefilter. The standard predictive control is a particular case for $L_o = \beta$.

Fig. 5 compares the closed-loop poles and step responses of the exact multiple-input–multiple-output (MIMO) control (Fig. 3) and the equivalent SISO control (Fig. 4). In gray color, the closed-loop eigenvalues fit the root–locus curves of the equivalent SISO loop as the ratio L_m/L increases. Transients of both exact and equivalent controls are barely distinguishable. Hence, the SISO control of Fig. 4 can be used to analyze the dynamic performance of the MIMO control, and, therefore, all classical control concepts, like bandwidth or phase and gain margins, apply, without the need for using the less-intuitive eigenvalue analysis of the MIMO loop. Stability properties of the control depend only on the equivalent feedback in Fig. 4, while the speed against reference changes depends on both prefilter and feedback loop.

C. SRF-RPCC With Sampling Before the Calculation Interval

As mentioned before, the condition for deadbeat operation is $t_d \approx T(m=1, \delta \approx 0)$. In this situation, the equivalent open-loop gain is, from Fig. 4

$$H_e(z) = \frac{L_m L_o}{L} \cdot \frac{1}{(z+L_o)(z-1)} \tag{30}$$

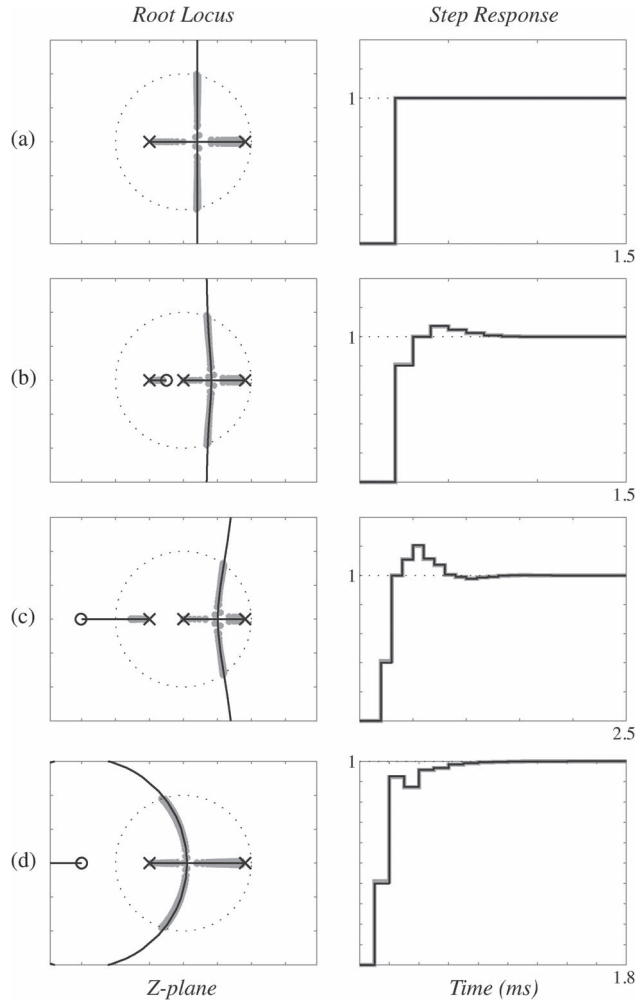

Fig. 5. Root–locus and step transient response of the proposed SRF-RPCC ($L = 1.9$ mH, $r_L = 1.5\ \Omega$). Switching and sampling frequencies are 10 kHz, and $L_o = 0.5$. (a) Ideal RPCC ($m = 1, \delta = 0$). (b) Adding a small delay ($m = 1, \delta = 0.2$). (c) Adding a larger delay ($m = 1, \delta = 0.6$). (d) Sampling inside the calculation interval with large delay ($m = 0, \delta = 0.6$).

where, for the sake of simplicity, it has been supposed that $\beta \approx 1$. The closed-loop characteristic equation is $P(z) = z^2 + (L_o - 1)\cdot z + L_o((L_m/L) - 1) = 0$. In order to find the limits for L_m, we will use the Jury criterion. The system is stable if $L_o|(L_m/L) - 1| < 1$, $P(z=1) > 0$ and $P(z=-1) > 0$. Expanding these inequations, we get that the control is stable if

$$0 < \frac{L_m}{L} < \frac{1+L_o}{L_o} = \left(\frac{L_m}{L}\right)_{\max}. \tag{31}$$

For $L_o = 1$ (traditional predictive control), the limit is the well-known $L_m = 2L$. A smaller value for L_o expands the tolerance against uncertainties in L while maintaining the deadbeat performance. For instance, if $L_o = 0.5$, the limit is $L_m = 3L$.

The frequency response of the equivalent loop gives an insight into the robustness performance. Assuming $L_m \approx L$ in (30) and applying the Tustin or bilinear transform, we get

$$H_e(w) = \frac{\nu_c}{w} \cdot \frac{(1 - \frac{w}{2/T})^2}{1 + \frac{w}{\nu_p}} \tag{32}$$

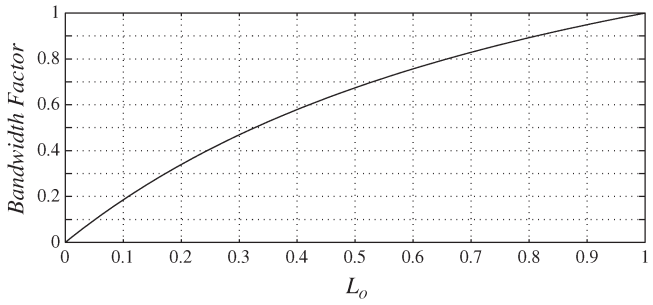

Fig. 6. Bandwidth-reduction factor of the proposed SRF-RPCC.

where $\nu_p = (2/T)((1 + L_o/1 - L_o)) > (2/T)$, and $\nu_c = (2/T)((L_o/2/1 + L_o))$ is the crossover frequency in the transformed w-domain. The real crossover frequency or control bandwidth of the proposed SRF-RPCC is

$$\omega_c = \frac{2}{T} \cdot \arctan\left(\frac{L_o/2}{1 + L_o}\right). \tag{33}$$

The bandwidth reduction factor, defined as

$$\alpha(L_o) \equiv \frac{\omega_c}{\omega_c(L_o \to 1)} \tag{34}$$

is shown in Fig. 6 as a function of L_o. The bandwidth ω_c reduces as L_o decreases, increasing both gain and phase margins. Moreover, the accelerated reference given by the derivative prefilter compensates for this bandwidth reduction (loss of velocity) of the feedback loop so that the control is still a two-sample deadbeat ($t_d \approx T$).

The phase margin is approximately

$$PM \approx \frac{\pi}{2} - 2\arctan\left(\frac{L_o/2}{1 + L_o}\right) - \arctan\left(\frac{L_o(1 - L_o)}{2(1 + L_o)^2}\right) \tag{35}$$

and, obviously, the gain margin is, as stated by (31)

$$GM(\text{dB}) = 20 \cdot \log\left(\frac{1 + L_o}{L_o}\right). \tag{36}$$

In general, the SRF-RPCC improves considerably the stability margins of the traditional predictive controllers. For instance, for $L_o = 0.4$, the phase margin of the SRF-RPCC with sampling before the calculation interval is 70°. Within the next section, it will be shown that the phase margin can be improved even more by sampling during the calculation interval.

If a nonnegligible delay T_d is considered now, the equivalent loop is actually

$$H_e(z) = \frac{L_m L_o}{L} \cdot \frac{(1 - \delta)z + \delta}{z(z + L_o)(z - 1)} \tag{37}$$

and the deadbeat performance degrades, as shown in Fig. 5(b) and (c). If $L_m \approx L$, the closed-loop characteristic polynomial is $z^3 - (1 - L_o)z^2 - L_o\delta z + L_o\delta$. Again, using the Jury criterion, we conclude that the control is stable if

$$\delta < \frac{1}{L_o} - \frac{1}{2}. \tag{38}$$

While the conventional predictive control only permits $\delta < 0.5$, the SRF-RPCC increases the tolerance against delays.

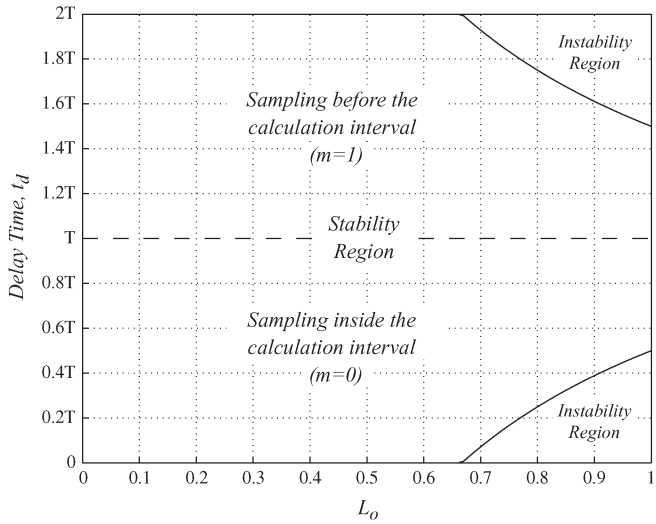

Fig. 7. Stability and instability regions of the proposed SRF-RPCC, as a function of the control delay t_d and L_o.

Now, even if the zero lies at the left of -1 (nonminimum phase zero) due to a large delay, the root–locus branch connects $-L_o$ with the zero. If the previous condition is satisfied (always, for $L_o < 2/3$), the closed-loop pole will remain in the stability region, in the interval $[-1, -L_o]$ [see Fig. 5(c)]. In fact, such an election of L_o sets the equivalent loop bandwidth below the frequency of the nonminimum phase zero. Again, the derivative prefilter compensates for the lack of speed of the loop.

D. SRF-RPCC With Sampling During the Calculation Interval

Robustness can be improved even more if sampling is performed inside the calculation interval. From Fig. 4, the equivalent loop transfer function is now

$$H_e(z) = \frac{L_m L_o}{L} \cdot \frac{(1 - \delta)z + \delta}{(z + L_o)(z - 1)}. \tag{39}$$

Applying the Jury criterion to the closed-loop characteristic polynomial, it is concluded that the control will be stable if the two following inequations are accomplished:

$$\frac{L_m}{L} \cdot (1 - 2\delta) < \frac{2(1 - L_o)}{L_o} \tag{40}$$

$$\frac{L_m}{L} < \frac{1 + L_o}{\delta L_o}. \tag{41}$$

Inequation (40) is equivalent to $|H_e(z = -1)| < 1$ (attenuation at high frequencies). To study the delay tolerance of the SRF-RPCC, it is assumed that $L_m \approx L$. In this case, (41) is always accomplished, and, from (40), we get the stability condition

$$\delta > \frac{3}{2} - \frac{1}{L_o}. \tag{42}$$

Conditions (38) and (42) are shown simultaneously in Fig. 7. If $L_o > 2/3$ (as occurs with the conventional predictive control), there are alternating stable/unstable episodes as long as the delay increases. However, if $L_o < 2/3$ is chosen, the SRF-RPCC is stable for any delay t_d in $[0, 2T]$ [see Fig. 5(d)].

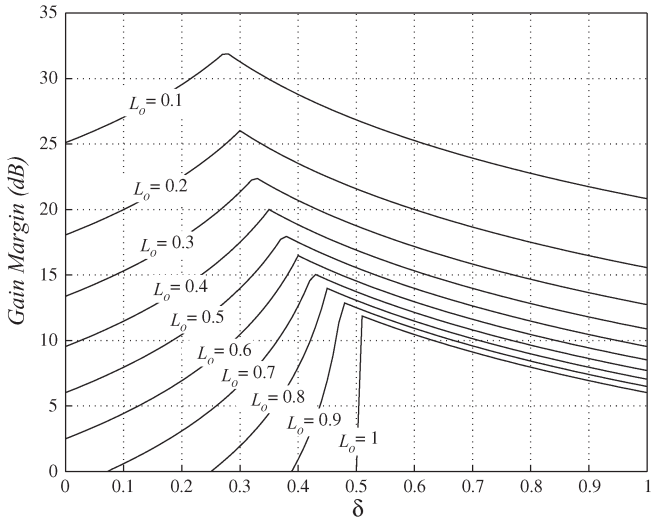

Fig. 8. Gain margin or L_m/L maximum ratio (db) of the SRF-RPCC when sampling inside the calculation interval ($m = 0$).

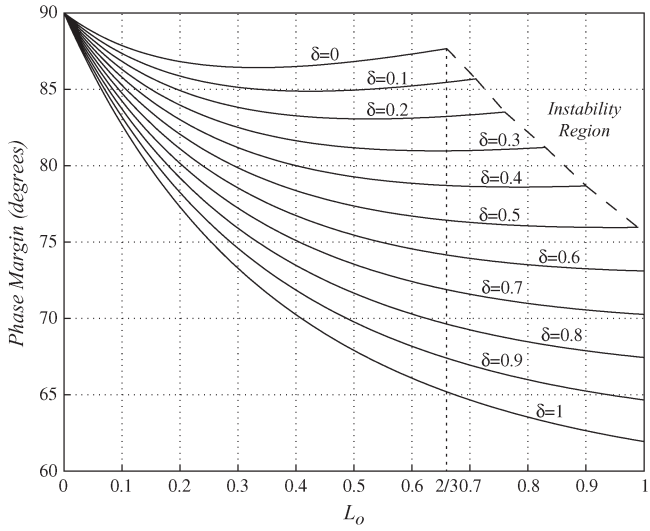

Fig. 9. Approximated phase margin of the SRF-RPCC, in degrees, when sampling inside the calculation interval ($m = 0$).

Tolerance to a higher delay time will be determined by the phase margin and the loop gain crossover frequency.

Stability limits for L_m/L can be also deduced from (40) and (41). Since (40) is always true for $\delta > 1/2$, the gain margin can be expressed as

$$GM = \left(\frac{L_m}{L}\right)_{\max} = \begin{cases} \min(a,b), & \text{if } \delta \in \left[0, \frac{1}{2}\right] \\ b, & \text{if } \delta \in \left[\frac{1}{2}, 1\right] \end{cases} \quad (43)$$

where $a = 2(1 - L_o)/(L_o(1 - 2\delta))$ and $b = (1 + L_o)/(\delta L_o)$. Equation (43) is represented in decibels in Fig. 8. The limits for L_m are considerably expanded here. For instance, if $L_o = 0.5$, $\delta = 0.5$, the limit is $L_m = 6L$, which is three times higher than the limits of the traditional predictive control. This limits can be increased even more if a smaller value of L_o is chosen.

To analyze the frequency response of the loop, we perform the bilinear transformation in (39), obtaining

$$H_e(w) = \frac{\nu_c}{w} \cdot \frac{\left(1 - \frac{w}{2/T}\right)\left(1 + \frac{w}{\nu_z}\right)}{1 + \frac{w}{\nu_p}} \quad (44)$$

where $\nu_z = (2/T)((1/1 - 2\delta))$, and ν_c and ν_p are those defined in the previous section. The bandwidth of the RPCC with sampling inside the calculation interval is still (33). As expected, the bandwidth is not delay-dependent, and Fig. 6 is still valid to determine the bandwidth reduction as a function of L_o.

The phase margin is approximately

$$PM \approx \frac{\pi}{2} - \arctan\left(\frac{L_o/2}{1 + L_o}\right) - \arctan\left(\frac{L_o(1 - L_o)}{2(1 + L_o)^2}\right) + \arctan\left(\frac{L_o\left(\frac{1}{2} - \delta\right)}{1 + L_o}\right) \quad (45)$$

which coincides with (35) for $\delta = 1$. The phase margin is represented in Fig. 9. For values $L_o < 2/3$, the control will always be stable, with attainable phase margins that easily exceed 75°. For instance, a design with $L_o = 0.5$ and $\delta = 0.5$ gives a phase margin of 77°.

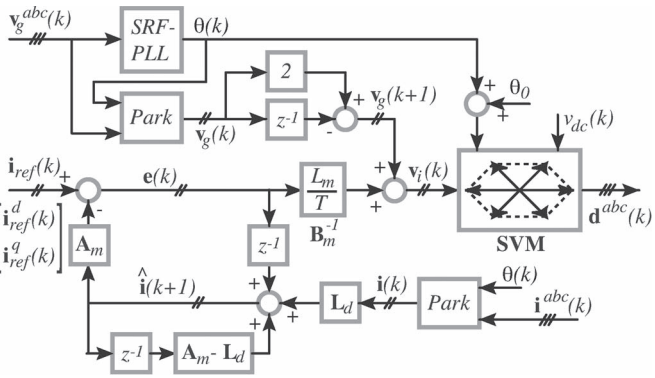

Fig. 10. Implemented SRF-RPCC algorithm.

V. Experimental Results

The proposed SRF-RPCC has been assayed on a 10-kW–10-kHz inverter, with $L = 1.9$ mH, $r_L = 1.5\ \Omega$, and dc-bus voltage $v_{\rm dc} = 560$ V built with a noncontrolled rectifier and a 2200-μF capacitor bank. A transformer with 1 : 2 turns ratio was used on the mains side. The measured efficiency was 94% at full power, and the total harmonic distortion was THD = 1.2%. The algorithm shown in Fig. 10 was programmed in an ARM-7 AT91SAM7X256 32-b microprocessor. A digital version of the SRF-phase-locked loop described in [21] permits the grid synchronization. Implementation of the space vector modulation (SVM) algorithm is described in [22].

Fig. 11 shows the three inverter output currents in steady state, for $L_o = 0.3$. Fluke i30s probes were used, with a 1-MΩ input impedance and a 100-mV/A sensitivity.

Fig. 12 shows one phase voltage (310 $V_{\rm pk}$) and the corresponding current (20 $A_{\rm pk}$). Power supplied to the grid is approximately 9300W. The duty-cycle SVM modulation is also displayed. The output filter lagging is compensated in Fig. 10 by advancing the SVM modulation by an angle θ_0.

Figs. 13 and 14 show the inverter output currents against the step changes in the amplitude and the phase references, respectively.

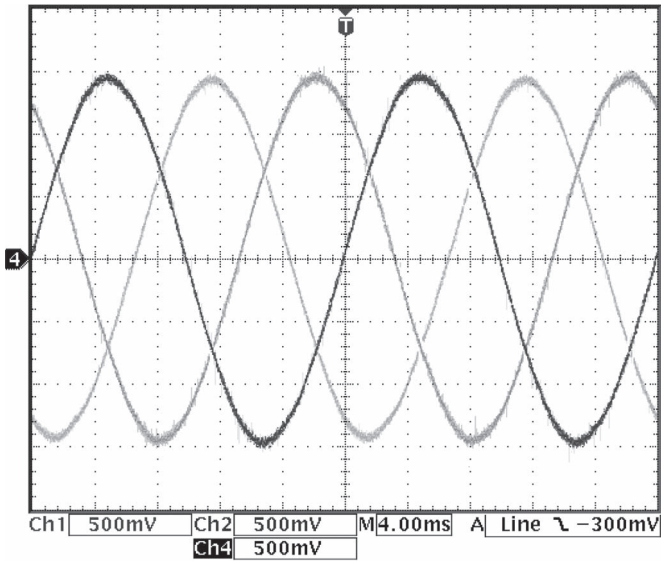

Fig. 11. Three-phase currents of the inverter with SRF-RPCC (5A/div).

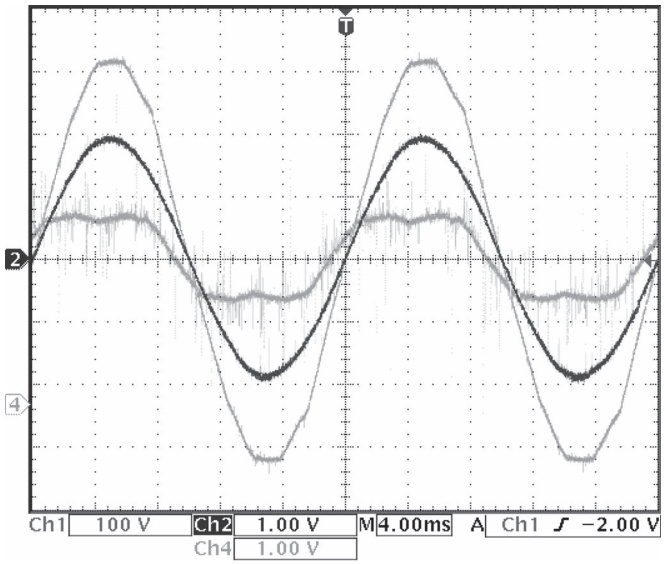

Fig. 12. (Ch.1, 100V/div.) Grid voltage, (Ch.2, 10A/div.) grid current, and (Ch.4) digital-to-analog converter output showing an SVM duty cycle.

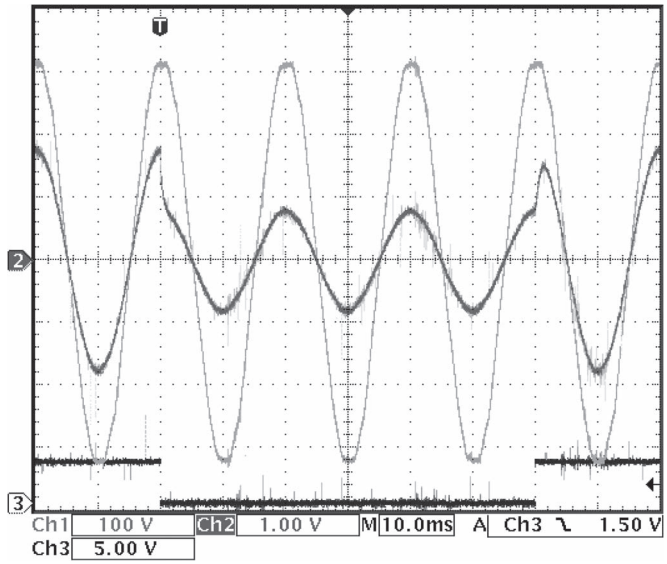

Fig. 13. Response of the inverter output current against step changes in the amplitude reference between 9 and 18A.

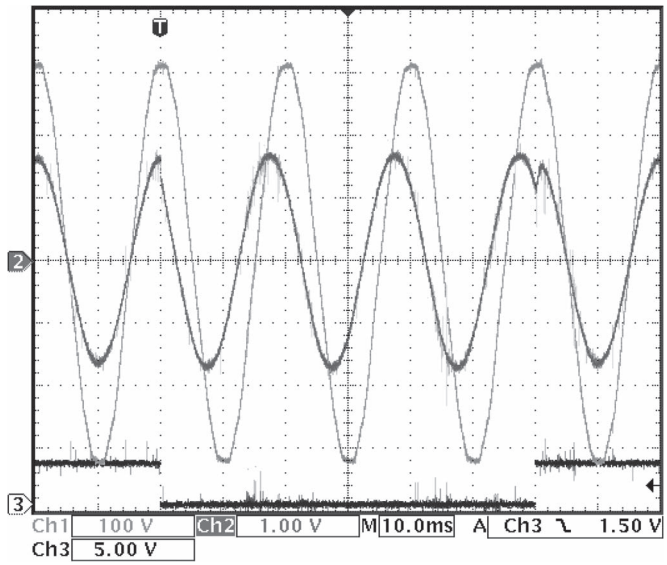

Fig. 14. Response of the inverter output current against step changes in the phase reference between 0° and 45°.

Fig. 15 shows the experimental transients in the inverter current produced by a step change in the amplitude reference for three different values of L_m/L. Data were captured and represented using Matlab. Sampling is outside the calculation interval $(m = 1)$ with $T_d = 10\ \mu$s $(\delta = 0.1)$, and $L_o = 0.3$. The control remains stable up to $L_m = 3L$, beyond the limit of the traditional predictive controller $L_m = 2L$.

Finally, Fig. 16 shows the improved limits achieved with the SRF-RPCC when sampling is inside the calculation interval. The control delay is $T_d = 48\ \mu$s. $(\delta = 0.48)$. The control remains stable up to $L_m/L \approx 8$, four times the limit of the traditional predictive controllers. The root–locus intersection with the unit circle (stability limit) in Fig. 5(d) is at higher frequency than in Fig. 5(c). This explains the higher frequency oscillations when sampling is inside the calculation interval.

VI. Conclusion

This paper has presented a new predictive current control (SRF-RPCC) for three-phase inverters in the synchronous or dq reference frame. This control offers the fastest possible current response while enhancing the stability limits of all previous predictive controllers against control delays and inductance variations. Active and reactive power can be independently and rapidly controlled (Figs. 13 and 14). The RPCC can be also applied to three-phase rectifiers with minimum changes.

This paper has started revealing that the d and q dynamics of the inverter currents are weakly coupled. Hence, the natural choice for any current controller is in a "diagonal" form so that the control decouples into two parallel SISO controls.

The SRF-RPCC combines a two-sample deadbeat control law with a diagonal observer to estimate the future value of the inverter output current. While the inclusion of an observer

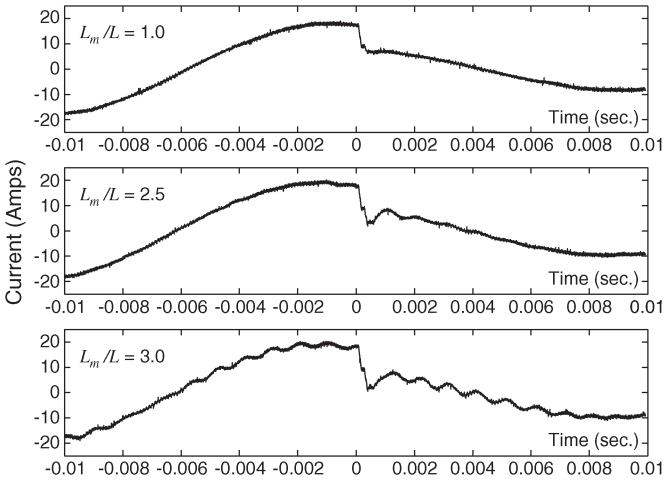

Fig. 15. Transients of the SRF-RPCC ($L_o = 0.3$) with sampling before the calculation interval ($m = 1$), $T_d = 10\ \mu$s ($\delta = 0.1$).

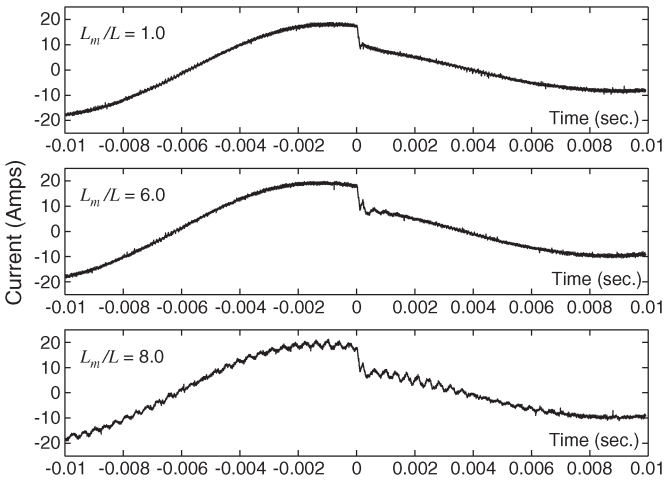

Fig. 16. Transients of the SRF-RPCC ($L_o = 0.3$) with sampling inside the calculation interval ($m = 0$), $T_d = 48\ \mu$s ($\delta = 0.48$).

typically degrades the stability margins, this is an exception to the rule. The observer gain L_o acts as a trimmer for robustness. Smaller values of L_o give larger phase and gain margins. This paper has used the equivalent SISO control to obtain relationships between L_o, delay time, and the stability margins obtained (Figs. 8 and 9), proving that this margins widely improve those of the previous predictive controllers.

This paper has also analyzed the stability limits of the RPCC against control delays as a function of L_o (Fig. 7). Unlike the typical predictive controllers, the RPCC is always stable against delays in the interval $[0, 2T]$ if $L_o < 2/3$ is chosen.

The key factor why the RPCC improves robustness is that the filtering properties of the observer reduce the loop gain at high frequencies [see (40)], while an equivalent derivative prefilter (Fig. 4) compensates the control bandwidth reduction (loss of speed) with an "accelerated" reference.

Notice that small values of L_o turn the error signal more dependent on current estimation than on current measurements (Fig. 10), and, therefore, a more accurate determination of L and r_L is needed in these cases. However, control tuning is straightforward for L_o between 0.3 and $\beta \approx 1$. This paper has shown experimental results for $L_o = 0.3$.

REFERENCES

[1] J. Carrasco, L. Franquelo, J. Bialasiewicz, E. Galvan, R. PortilloGuisado, M. Prats, J. Leon, and N. Moreno-Alfonso, "Power-electronic systems for the grid integration of renewable energy sources: A survey," *IEEE Trans. Ind. Electron.*, vol. 53, no. 4, pp. 1002–1016, Jun. 2006.

[2] J. Schonberger, R. Duke, and S. Round, "DC-bus signaling: A distributed control strategy for a hybrid renewable nanogrid," *IEEE Trans. Ind. Electron.*, vol. 53, no. 5, pp. 1453–1460, Oct. 2006.

[3] M. Prodanovic and T. Green, "High-quality power generation through distributed control of a power park microgrid," *IEEE Trans. Ind. Electron.*, vol. 53, no. 5, pp. 1471–1482, Oct. 2006.

[4] E. Figueres, G. Garcera, J. Sandia, F. Gonzalez-Espin, and J. Rubio, "Sensitivity study of the dynamics of three-phase photovoltaic inverters with an LCL grid filter," *IEEE Trans. Ind. Electron.*, vol. 56, no. 3, pp. 706–717, Mar. 2009.

[5] R. Gonzalez, E. Gubia, J. Lopez, and L. Marroyo, "Transformerless single-phase multilevel-based photovoltaic inverter," *IEEE Trans. Ind. Electron.*, vol. 55, no. 7, pp. 2694–2702, Jul. 2008.

[6] S. Alepuz, S. Busquets-Monge, J. Bordonau, J. Gago, D. Gonzalez, and J. Balcells, "Interfacing renewable energy sources to the utility grid using a three-level inverter," *IEEE Trans. Ind. Electron.*, vol. 53, no. 5, pp. 1504–1511, Oct. 2006.

[7] B. Sahan, A. Vergara, N. Henze, A. Engler, and P. Zacharias, "A single-stage PV module integrated converter based on a low-power current-source inverter," *IEEE Trans. Ind. Electron.*, vol. 55, no. 7, pp. 2602–2609, Jul. 2008.

[8] A. Ristow, M. Begovic, A. Pregelj, and A. Rohatgi, "Development of a methodology for improving photovoltaic inverter reliability," *IEEE Trans. Ind. Electron.*, vol. 55, no. 7, pp. 2581–2592, Jul. 2008.

[9] F. Blaabjerg, R. Teodorescu, M. Liserre, and A. Timbus, "Overview of control and grid synchronization for distributed power generation systems," *IEEE Trans. Ind. Electron.*, vol. 53, no. 5, pp. 1398–1409, Oct. 2006.

[10] Y.-R. Mohamed and E. El-Saadany, "A control scheme for PWM voltage-source distributed-generation inverters for fast load-voltage regulation and effective mitigation of unbalanced voltage disturbances," *IEEE Trans. Ind. Electron.*, vol. 55, no. 5, pp. 2072–2084, May 2008.

[11] Q. Zeng and L. Chang, "An advanced SVPWM-based predictive current controller for three-phase inverters in distributed generation systems," *IEEE Trans. Ind. Electron.*, vol. 55, no. 3, pp. 1235–1246, Mar. 2008.

[12] Y.-R. Mohamed and E. El-Saadany, "An improved deadbeat current control scheme with a novel adaptive self-tuning load model for a three-phase PWM voltage-source inverter," *IEEE Trans. Ind. Electron.*, vol. 54, no. 2, pp. 747–759, Apr. 2007.

[13] J. Rodriguez, J. Pontt, C. A. Silva, P. Correa, P. Lezana, P. Cortes, and U. Ammann, "Predictive current control of a voltage source inverter," *IEEE Trans. Ind. Electron.*, vol. 54, no. 1, pp. 495–503, Feb. 2007.

[14] H. Abu-Rub, J. Guzinski, Z. Krzeminski, and H. Toliyat, "Predictive current control of voltage-source inverters," *IEEE Trans. Ind. Electron.*, vol. 51, no. 3, pp. 585–593, Jun. 2004.

[15] G. Bode, P. C. Loh, M. Newman, and D. Holmes, "An improved robust predictive current regulation algorithm," *IEEE Trans. Ind. Appl.*, vol. 41, no. 6, pp. 1720–1733, Nov./Dec. 2005.

[16] T. Summers and R. Betz, "Dead-time issues in predictive current control," *IEEE Trans. Ind. Appl.*, vol. 40, no. 3, pp. 835–844, May/Jun. 2004.

[17] P. Mattavelli, "An improved deadbeat control for ups using disturbance observers," *IEEE Trans. Ind. Electron.*, vol. 52, no. 1, pp. 206–212, Feb. 2005.

[18] R. A. Mastromauro, M. Liserre, and A. Dell'Aquila, "Study of the effects of inductor nonlinear behavior on the performance of current controllers for single-phase PV grid converters," *IEEE Trans. Ind. Electron.*, vol. 55, no. 5, pp. 2043–2052, May 2008.

[19] J. C. Moreno, J. M. Espi Huerta, R. G. Gil, and S. A. Gonzalez, "A robust predictive current control for three-phase grid-connected inverters," *IEEE Trans. Ind. Electron.*, vol. 56, no. 6, pp. 1993–2004, Jun. 2009.

[20] H. Kojabadi, B. Yu, I. Gadoura, L. Chang, and M. Ghribi, "A novel DSP-based current-controlled PWM strategy for single phase grid connected inverters," *IEEE Trans. Power Electron.*, vol. 21, no. 4, pp. 985–993, Jul. 2006.

[21] V. Kaura and V. Blasko, "Operation of a phase locked loop system under distorted utility conditions," *IEEE Trans. Ind. Appl.*, vol. 33, no. 1, pp. 58–63, Jan./Feb. 1997.

[22] J.-O. Krah and J. Holtz, "High-performance current regulation and efficient PWM implementation for low-inductance servo motors," *IEEE Trans. Ind. Appl.*, vol. 35, no. 5, pp. 1039–1049, Sep./Oct. 1999.

José M. Espí Huerta (M'98) received the M.Sc. degree in physics, with specialization in electronics, and the Ph.D. degree in electrical engineering from the University of Valencia, Valencia, Spain, in 1992 and 1998, respectively.

He was with the R&D Department of GH Electrotermia, where he was involved with induction heating generators design. He worked for two years with the Power Conditioning Section of the European Space Research and Technology Center, European Space Agency, in Noordwijk, The Netherlands. Since 1999, he has been an Associate Professor in the Electronics Engineering Department, University of Valencia, and a member of the Laboratory of Industrial Electronics and Instrumentation (LEII).

Jaime Castelló-Moreno (S'08) received the B.S. degree in telecommunications engineering and the M.S. degree in electrical engineering from the University of Valencia, Valencia, Spain, in 1999 and 2004, respectively.

He is currently a Laboratory Officer in the Electronics Engineering Department, University of Valencia. His fields of interest are power electronics, control systems, and signal processing.

Jonatan Roberto Fischer received the B.S. degree in electronics engineering from the Universidad Nacional de Mar del Plata (UNMdP), Mar del Plata, Argentina, in 2008, where he is currently working toward the Ph.D. degree.

His research interests are power electronics, control systems, and digital signal processing.

Rafael García-Gil received the M.Sc. degree in physics and the M.Sc. and Ph.D. degrees in electronics engineering from the University of Valencia, Valencia, Spain, in 1993, 1995, and 2002, respectively.

He was with the European Organization for Nuclear Research (CERN), Geneva, Switzerland, for two years. From 1996 to 1998, he was with Computadores, Redes e Ingeniería, S.A. (CRISA), where he was involved in the design of power converters for aerospace applications. Since the end of 1998, he has been with the Electronics Engineering Department, University of Valencia, where he is currently an Associate Professor.